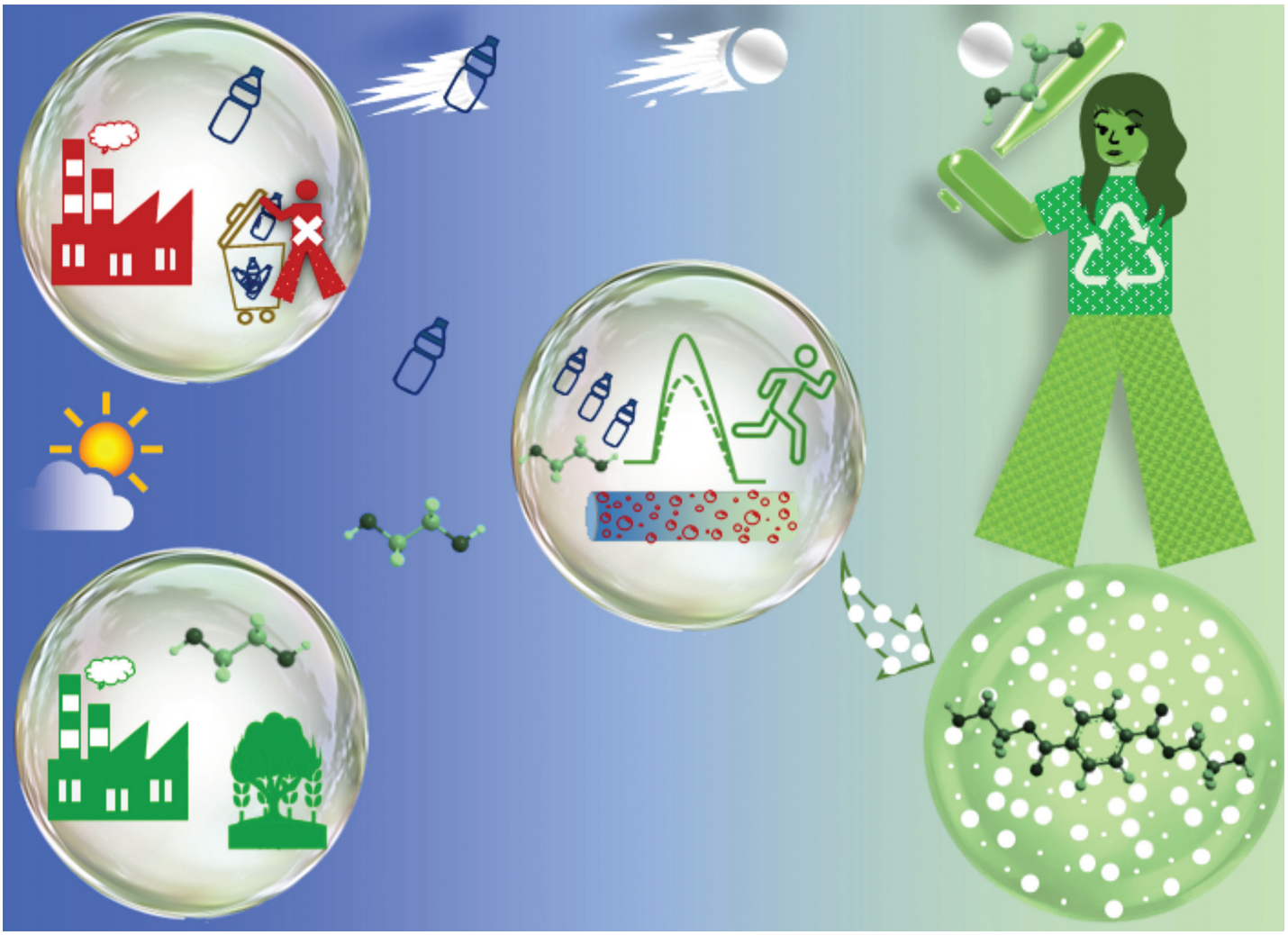

Showcasing research from Professor Putla Sudarsanam's laboratory, Department of Chemistry, Indian Institute of Technology Hyderabad, Kandi 502284, Telangana, India.

Morphology-tuned MnO_x/TiO_2 nanocatalysts for recycling PET plastic waste using biomass-derived ethylene glycol

The study elucidated the efficient recycling of PET waste using a cost-effective and sustainable MnO_x/TiO_2 nanocatalyst. The synergy of MnO_x nanoparticles with TiO_2 nanorods led to surface-enriched basic sites and electron-deficient Mn^{3+}/Mn^{2+} species with a significant effect on activating ethylene glycol and PET ester linkages, respectively, towards the formation of a highly valuable monomer for the plastic industry, reducing the use of fossil-derived precursors. The morphology-tuned catalyst design concept could pave the way for developing new heterogeneous catalytic materials and practically viable catalytic processes for the circular plastic economy.

Image reproduced by permission of Putla Sudarsanam.

As featured in:

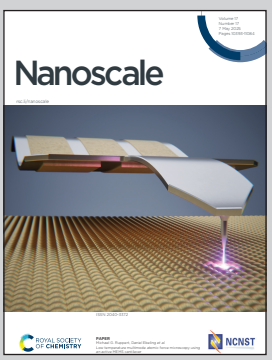

See Bhattu Swapna and Putla Sudarsanam, *Nanoscale*, 2025, **17**, 10620.

ROYAL SOCIETY OF CHEMISTRY

rsc.li/nanoscale

Registered charity number: 207890

Nanoscale

ROYAL SOCIETY OF CHEMISTRY

PAPER

View Article Online
View Journal | View Issue

Cite this: *Nanoscale*, 2025, **17**, 10620

Morphology-tuned MnO_x/TiO_2 nanocatalysts for recycling PET plastic waste using biomass-derived ethylene glycol†

Bhattu Swapna,[a] Madam Bobby Barnabas,[a] Pragya Moni Gogoi,[b] Pankaj Bharali,[b] Giridhar Madras[c] and Putla Sudarsanam *[a]

This study presents a decisive role of TiO_2 morphology on the catalytic activity of MnO_x/TiO_2 nanomaterials for the chemical recycling of PET waste bottles using biomass-derived ethylene glycol to produce a valuable monomer, bis(2-hydroxyethyl) terephthalate (BHET). Three types of MnO_x/TiO_2 nanocatalysts were prepared by varying the TiO_2 morphology (nanosheets: NS, nanotubes: NT, and nanorods: NR). The combination of MnO_x nanoparticles and TiO_2 nanorods (MnO_x/TiO_2-NR) showed significantly enhanced catalytic activity in PET glycolysis, with a 91% isolated yield of BHET at 190 °C in 3 h, whereas 74% and 82% yields of BHET were attained with MnO_x/TiO_2-NS and MnO_x/TiO_2-NT nanocatalysts, respectively. The morphology of TiO_2 and the uniform dispersion of MnO_x on TiO_2-NR were confirmed by electron microscopic analysis. The MnO_x/TiO_2-NR catalyst contains optimum basic sites, which play a key role, along with surface hydroxyl species and Mn^{3+}/Mn^{2+} species, in activating ethylene glycol and PET/its oligomers towards BHET formation. The excellent stability of the MnO_x/TiO_2-NR nanocatalyst, as confirmed by the hot-filtration test, good catalytic reusability up to four cycles, non-toxic nature, and the low cost of the MnO_x/TiO_2 materials indicate the practical feasibility of the developed catalytic protocol for the plastic recycling industry.

Received 20th December 2024,
Accepted 8th February 2025

DOI: 10.1039/d4nr05373g

rsc.li/nanoscale

1. Introduction

Plastic is used widely because of its low cost, durability, and wide-range of applications.[1–3] However, the use of plastic generates vast amounts of waste and causes environmental pollution. Current recycling processes only manage to recycle 9% of the plastic waste into valuable materials and chemicals, with the rest ending up in landfills or being incinerated.[4–11] Among various plastics, polyethylene terephthalate (PET) is the most used polyester plastic due to its consistent properties and numerous applications.[12–14] Recycling PET waste into materials, monomers, and chemicals is essential for mitigating plastic pollution and reducing the use of fossil feedstock to produce polyester-based materials.[15–17] Recycling one ton of PET can save ~5.6 barrels of oil that would otherwise be used to produce virgin PET polymers.[18,19]

Mechanical and chemical recycling methods have been widely investigated for PET waste valorization.[20,21] Mechanical recycling can transform PET waste bottles into new plastic products with minimal changes to the chemical structure. However, this time-consuming method needs multiple steps, resulting in low-quality products.[21,22] In contrast, chemical recycling is an efficient process for transforming PET waste into high-quality products under mild conditions.[22–24] PET glycolysis using biomass-derived ethylene glycol (EG) is both a cost-effective and environmentally sustainable process to produce bis(2-hydroxyethyl) terephthalate (BHET), a vital monomer for various plastic products.[22,25] EG can be produced in greater quantities through the catalytic hydrogenolysis of renewable cellulosic biomass.[26,27] Catalysts are essential for activating the ester bonds in PET and the hydroxyl groups in EG during the glycolysis reaction to achieve higher yields of the BHET monomer.[22,28–32] In this regard, applying low-cost and efficiently recyclable heterogeneous catalysts can provide industrially compatible methods for PET recycling, thus promoting the circular plastic economy (Fig. 1).

Nanostructured metal oxide-based catalysts are particularly effective for heterogeneous catalysis, including plastic waste recycling, due to their size and shape-tunable surface chemistry,

[a]*Department of Chemistry, Indian Institute of Technology Hyderabad, Kandi 502284, Telangana, India. E-mail: sudarsanam.putla@chy.iith.ac.in*
[b]*Department of Chemical Sciences, Tezpur University, Napaam 784028, Assam, India*
[c]*Department of Chemical Engineering, Indian Institute of Technology Hyderabad, Kandi 502284, Telangana, India*

†Electronic supplementary information (ESI) available: TEM images of TiO_2-NS and TiO_2-NT, N_2 adsorption-desorption isotherms, BET surface area, pore size, and pore volume of the catalysts, NMR spectra and HR-MS analysis of BHET, and XPS analysis of fresh and spent MnO_x/TiO_2-NR catalysts. See DOI: https://doi.org/10.1039/d4nr05373g

higher surface area, and abundant acid–base sites.[33–36] The shape-tuning of metal oxide particles can optimize the coordination geometry of metal and oxygen sites, along with more surface-exposed sites like edges, corners, and kinks, which can provide a high concentration of selective active sites for achieving enhanced catalytic activity with desirable products. Titanium dioxide (TiO_2) is a commonly used support material for anchoring catalytically active sites for various energy and environmental applications.[37–40] The surface features/geometries, defects, and crystalline phases (anatase and rutile) of TiO_2 nanomaterials can control the adsorption/activation of reactants/intermediates, influencing reaction pathways and catalytic performance. The morphology of TiO_2, including nanosheets, nanotubes, and nanorods, offers distinct advantages in heterogeneous catalysis due to variations in surface area, exposed facets, and unsaturated surface-Ti^{x+} sites. Controlling these morphologies and elucidating their role in the structure–activity properties of nanocatalysts can offer potential strategies to advance the heterogeneous catalysis field for plastic waste recycling applications.

Manganese oxides (MnO_x) are widely utilized in heterogeneous catalysis due to their low cost, diverse crystal structures, multiple oxidation states, and facile redox Mn sites.[21,34,41,42] These characteristics make MnO_x a versatile catalyst for various acid–base and redox reactions.[43] Our recent work emphasized the catalytic role of a MnO_x nanomaterial for PET glycolysis.[43] The combination of MnO_x with redox metal oxides like TiO_2 can lead to synergistic properties with enhanced catalytic activity and selectivity for PET glycolysis. This combination inspired us to develop advanced MnO_x/TiO_2 nanocatalysts by varying the morphology of TiO_2 (nanosheets, nanotubes, and nanorods) for PET glycolysis using biomass-derived EG. The MnO_x catalyst supported on TiO_2 nanorods (NR) demonstrated superior catalytic performance, achieving a 91% isolated yield of BHET under mild conditions compared to the existing literature.[22,44] The structure–activity relationship of MnO_x/TiO_2 nanocatalysts was elucidated by comparing the properties of the catalysts investigated using various techniques (powder XRD, BET, XPS, TEM, STEM-EDAX, and CO_2-TPD) with catalytic activity data. The role of basic sites, surface hydroxyl groups, and Mn^{3+}/Mn^{2+} species in activating PET and EG was elucidated.

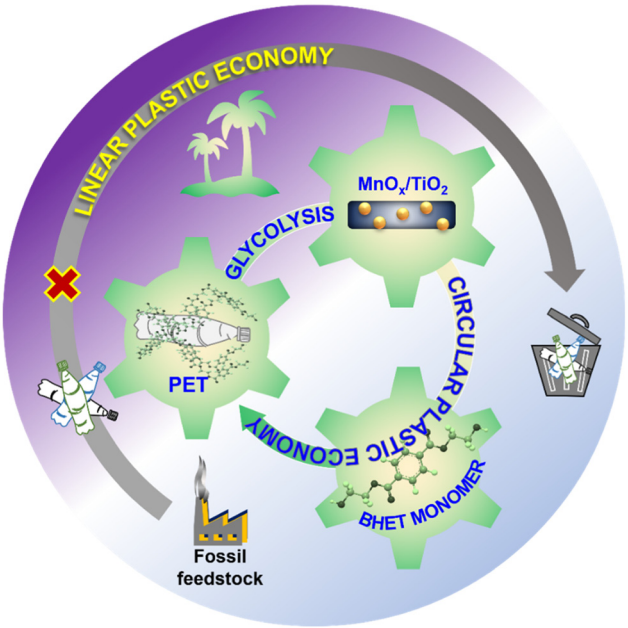

Fig. 1 Catalytic glycolysis of post-consumer PET bottles to the valuable BHET monomer towards the circular plastic economy.

Putla Sudarsanam

Dr Sudarsanam Putla is an Assistant Professor at the Department of Chemistry, Indian Institute of Technology Hyderabad, India. He completed his M.Sc. (Chemistry) at IIT Madras and Ph.D. at CSIR-IICT, Hyderabad. From 2014 to 2019, he worked as a postdoctoral fellow at RMIT University (Melbourne), LIKAT (Germany), and KU Leuven (Belgium). He has received several awards and fellowships, including the PECFAR award – 2023 (Indo-German Science & Technology Centre), the Associate Fellow of the Telangana Academy of Sciences – 2022, and the Australian Alumni Award – 2021. His research focuses on developing novel heterogeneous catalysts for plastic waste recycling and biomass valorization to fuels, monomers, and value-added chemicals. He has authored ~80 journal articles (h-index: 41, ~5800 citations), edited 4 books, and serves on editorial boards of ACS Sustainable Chemistry & Engineering, Molecular Catalysis, and Applied Catalysis O: Open journals.

2. Experimental section

2.1. Catalyst synthesis

2.1.1. Hydrothermal synthesis of shape-controlled TiO_2 nanomaterials. Three types of shape-controlled TiO_2 nanomaterials (nanosheets, nanotubes, and nanorods) were synthesized using hydrothermal methods. To prepare TiO_2 nanosheets (TiO_2-NS), anatase TiO_2 (Sigma Aldrich, 99.9%) was dispersed in 50 mL of 10 mol L^{-1} NaOH solution (Fig. 2).[42,45] The solution underwent 5 min of ultrasonication and was then transferred to a Teflon-lined autoclave reactor, which was heated at 130 °C for 3 h in an oven. After cooling to room temperature, the sample was treated by adding 200 mL of 0.1 mol L^{-1} HNO_3 and stirred for 3 h. The mixture was then centrifuged multiple times with deionized water until the pH was stabilized at 7. The resulting solid was oven-dried at 100 °C for 12 h and subsequently calcined at 300 °C for 4 h to yield the TiO_2-NS material.

A similar hydrothermal method with modifications was used for synthesizing TiO_2 nanotubes (TiO_2-NT) and nanorods (TiO_2-NR).[40,46] Anatase TiO_2 powder (Sigma Aldrich, 99.9%) was dispersed in 5 mL of distilled water and ultrasonicated for 5 min, followed by the gradual addition of 70 mL of NaOH solution (10 mol L^{-1}) over a period of 10 min (Fig. 2). After stirring for 30 min, the solution was treated in a hydrothermal autoclave at 140 °C for 20 h in an oven. The solid product was centrifuged several times using a dilute HNO_3 solution (0.1 mol L^{-1}) and deionized water until the pH reached 7. The solid sample was oven-dried at 100 °C for 12 h and then calcined at 400 °C and 500 °C for 4 h to obtain TiO_2-NT and TiO_2-NR materials, respectively.

2.1.2. Wetness-impregnation synthesis of MnO_x/TiO_2 nanocatalysts. The synthesized shape-controlled TiO_2 nanomaterials (NS, NT, and NR) were used as the supports for preparing the MnO_x/TiO_2 nanocatalysts by a simple wetness-impregnation method. The required amount of $KMnO_4$ precursor (20 wt% Mn on TiO_2) was dissolved in deionized water, and the respective shape-controlled TiO_2 was added at room temperature. The solution temperature was increased to 65 °C under mild magnetic stirring and the temperature was maintained for 1 h. Then, the temperature was increased to 95 °C under continuous stirring until all the solvent was evaporated. The sample was oven-dried at 100 °C for 12 h and calcined at 400 °C for 4 h. The obtained catalysts are denoted by MnO_x/TiO_2-NS, MnO_x/TiO_2-NT, and MnO_x/TiO_2-NR (Fig. 2).

2.2. Characterization studies of the TiO_2 and MnO_x/TiO_2 nanocatalysts

The details are provided in the ESI.†

2.3. Reaction procedure for PET glycolysis

Used PET plastic bottles were washed with soap water and acetone to remove the impurities. The cleaned bottles were then cut into small pieces of ~3 mm for the reaction, which was conducted at 190 °C for 3 h using the required amounts of PET, EG, and catalyst. After the reaction, the mixture was filtered to remove unreacted PET and catalyst. The filtrate was heated to 70 °C and stirred for 1 h to achieve supersaturation of the solvent, and then placed in a refrigerator for 24 h to obtain BHET monomer crystals.

The conversion of PET and BHET yield were estimated using the following equations, wherein W_i and W_f are the initial and final weights of PET, respectively.

$$\text{PET conversion}\,(\%) = \frac{W_i \text{ of PET} - W_f \text{ of PET}}{W_i \text{ of PET}} \times 100$$

$$\text{BHET yield}\,(\%) = \frac{\text{experimental yield of BHET}}{\text{theoretical yield of BHET}} \times 100$$

3. Results and discussion

3.1. TEM and powder XRD studies of TiO_2 and MnO_x/TiO_2 nanocatalysts

The effects of hydrothermal treatment and calcination temperature on the morphology of TiO_2 were confirmed by TEM analysis. The hydrothermal treatment at 130 °C for 3 h, followed by calcination at 300 °C for 4 h, gave the nanosheet morphology of TiO_2 (TiO_2-NS) with more than 1 micrometer size of side length (Fig. S1a, ESI†). In contrast, the hydrothermal treatment at 140 °C for 20 h, and then calcination at 400 °C and 500 °C for 4 h provided the nanotube (length = 55–235 nm and width = 9–12 nm, Fig. S1b, ESI†) and a major fraction of nanorod morphology particles (length = 35–174 nm and width = 7–9 nm, Fig. 3a), respectively. The TEM analysis of the most active MnO_x/TiO_2-NR catalyst (Fig. 3b and c) revealed the presence of TiO_2 nanorods, along with a few nanotubes and MnO_x nanoparticles (particle size of 6–11 nm). The STEM-EDAX

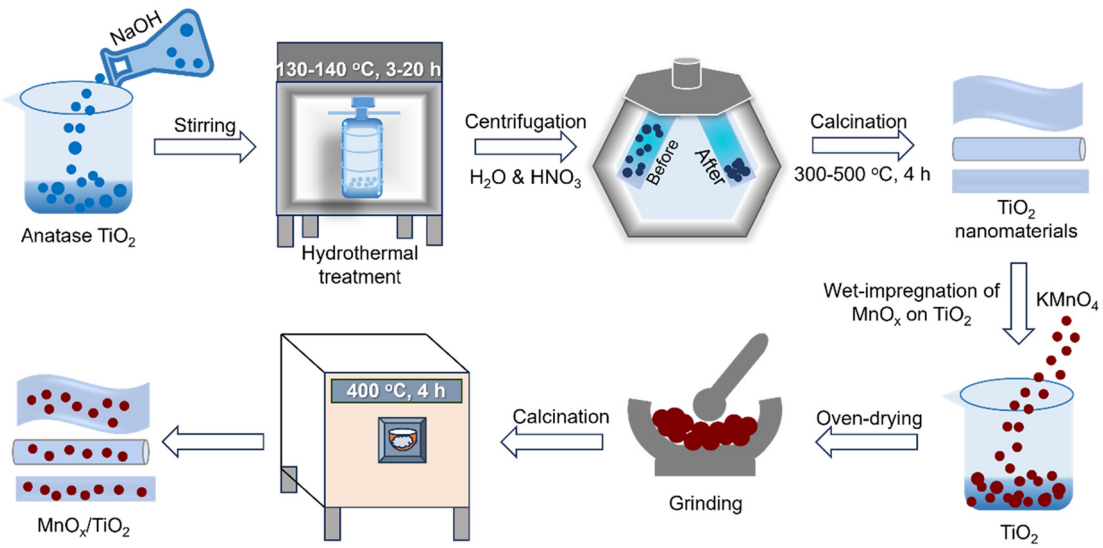

Fig. 2 The synthesis procedure of TiO_2 and MnO_x/TiO_2 nanocatalysts.

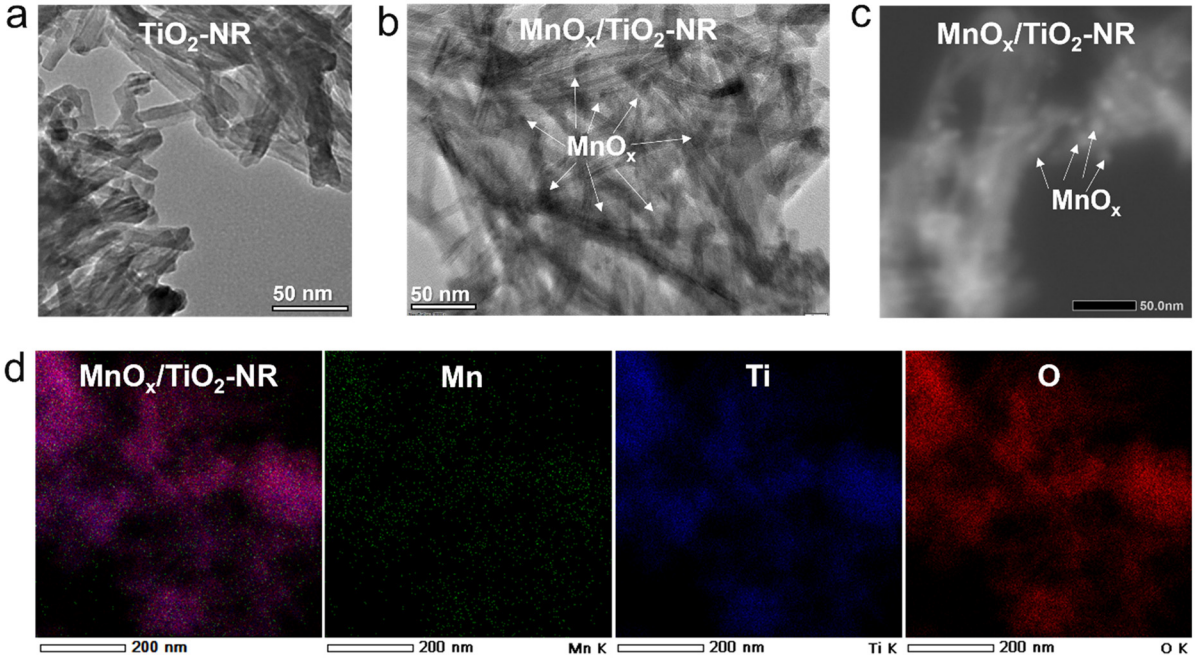

Fig. 3 Bright field TEM images of (a) TiO_2-NR and (b) MnO_x/TiO_2-NR catalysts. (c) Dark-field image of the MnO_x/TiO_2-NR catalyst. (d) STEM-EDAX elemental mapping images of the MnO_x/TiO_2-NR catalyst.

elemental mapping analysis shows the homogeneous dispersion of Mn species in the MnO_x/TiO_2-NR catalyst (Fig. 3d). The homogeneous dispersion of Mn species can provide uniform surface-active sites, which can play a favorable role in heterogeneous catalysis to achieve higher reaction rates with enhanced product selectivity, including PET glycolysis reaction.

The powder XRD analysis showed various sharp diffraction peaks at 2θ = 25.3, 36.7, 37.7, 38.5, 48.1, 53.7, 55.1, 62.6, 68.7, 70.2, and 75.2°, corresponding to the anatase phase of TiO_2 in all the materials[40,45,46] (Fig. 4a). Pristine TiO_2 nanomaterials exhibited a variation in the 2θ values of these peaks, attributed to the structural perturbations induced by the morphology of TiO_2 (Fig. 4b). Similar diffraction peaks of anatase TiO_2 were observed in MnO_x/TiO_2 nanocatalysts (Fig. 4a) with a noticeable peak shift compared to pristine TiO_2 nanomaterials (Fig. 4b). This shift indicates the interaction of MnO_x with TiO_2, leading to structural perturbations in the lattice of anatase TiO_2. Besides, the MnO_x/TiO_2 nanocatalysts have two diffraction peaks at 2θ = 12.3 and 28.8°, corresponding to the α-MnO_2 phase (JCPDS file no. 44-0141).[47]

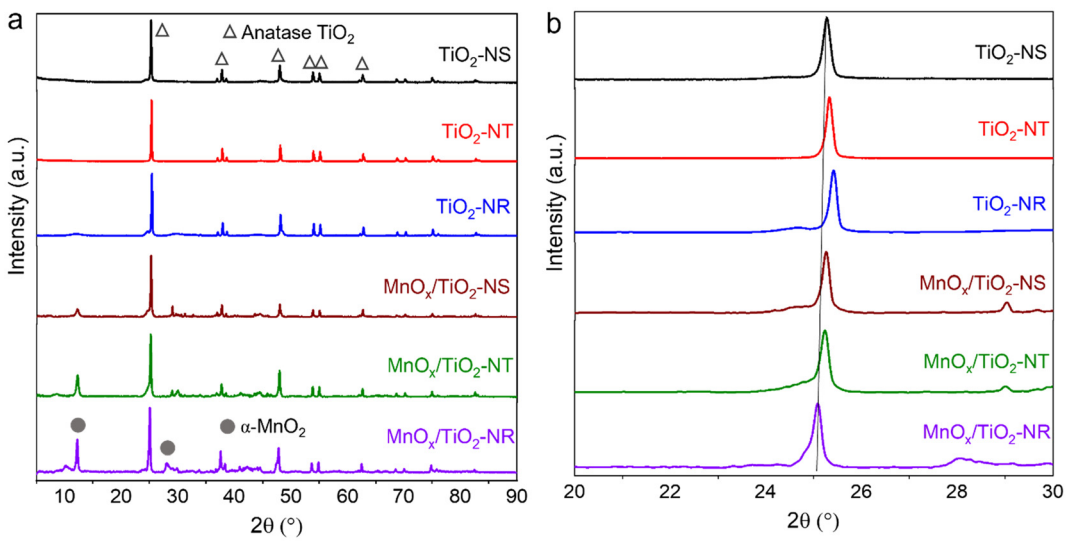

Fig. 4 (a) Powder XRD and (b) magnified powder XRD of TiO_2 and MnO_x/TiO_2 nanocatalysts.

3.2. XPS analysis of TiO_2 and MnO_x/TiO_2 nanocatalysts

XPS analysis was conducted to determine the oxidation states of Mn, Ti, and O species, as well as their interactions in the catalysts. The Mn 2p XP spectra exhibited two spin–orbit doublets, namely Mn $2p_{3/2}$ and Mn $2p_{1/2}$, with the corresponding peaks at 636.1–644.8 and 647.5–655.1 eV, respectively (Fig. 5a).[43,46,48–51] Deconvolution of the Mn $2p_{3/2}$ peak revealed two major peaks at 639.6–639.9 eV and 642.4–642.6 eV, indicating the presence of Mn^{2+} and Mn^{3+} oxidation states, respectively, with a major amount of Mn^{2+} in all MnO_x/TiO_2 catalysts.[40,46] The MnO_x/TiO_2-NR catalyst has a higher percentage of $Mn^{3+/2+}$ (71.8%) compared to the MnO_x/TiO_2-NS (15.8%) and MnO_x/TiO_2-NT (53.9%) catalysts. The $Mn^{3+/2+}$ is a strong redox couple, and the more electron-deficient Mn^{3+} species can interact with the oxygen of the PET ester groups, inducing their susceptibility to the attack of EG. Though the powder XRD analysis showed the presence of MnO_2 (Fig. 4a), using ultra-high vacuum conditions during XPS analysis can lead to the reduction of metal ions, which could be the reason for the absence of Mn^{4+} species in Mn 2p XPS spectra (Fig. 5a).[52,53] The Ti 2p XPS spectra showed Ti^{4+} species with two strong peaks around 457.2 and 463.1 eV, corresponding to Ti $2p_{3/2}$ and Ti $2p_{1/2}$, respectively (Fig. 5b).[54] Variation in BEs of the Ti^{4+} species was observed after adding MnO_x, indicating the strong Mn–Ti interaction. The O 1s spectra showed different types of oxygen species (Fig. 5c). The first peak around 527.1 eV represents lattice oxygen (O_L) bound to Ti^{4+} in

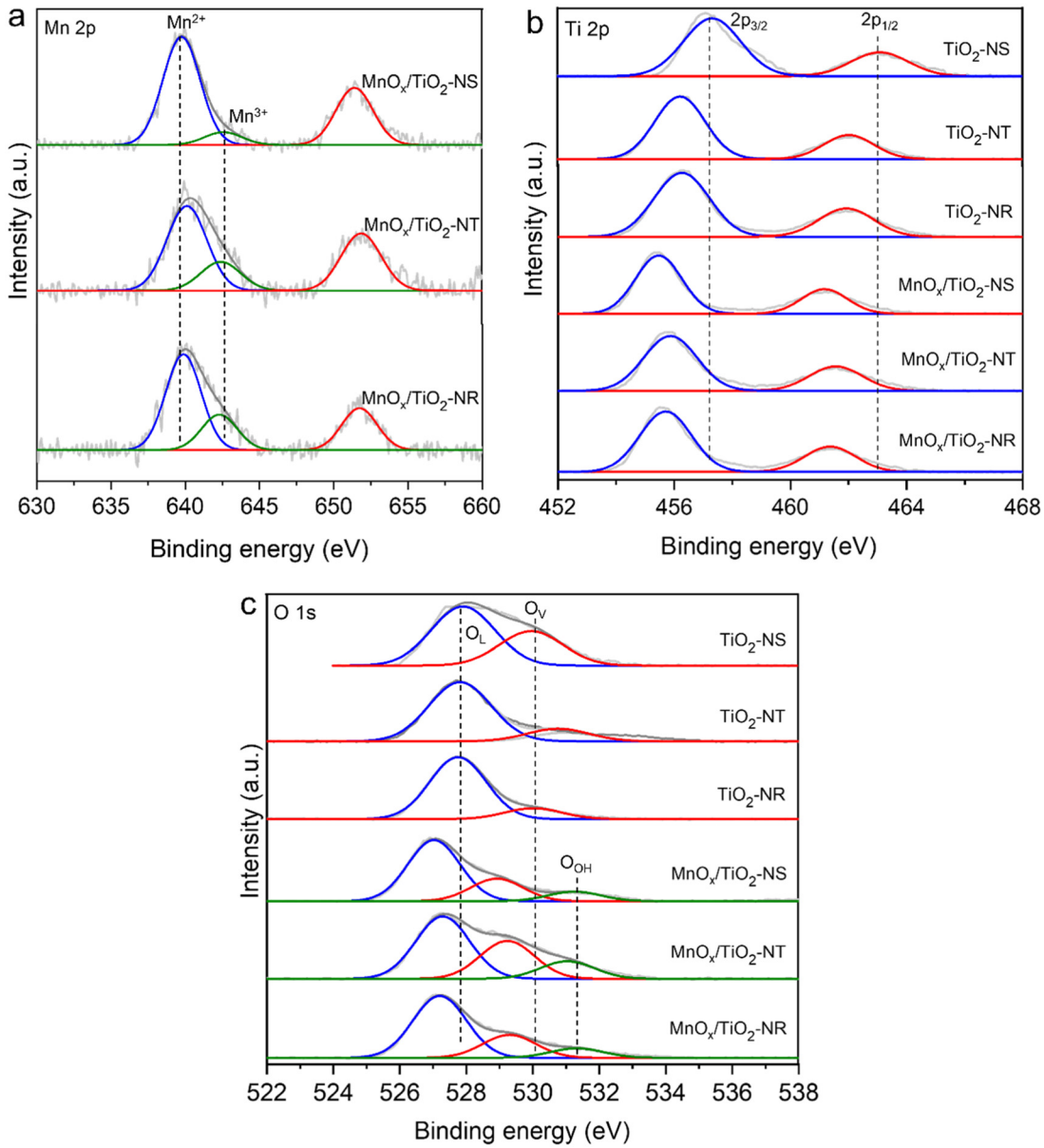

Fig. 5 (a) Mn 2p, (b) Ti 2p, and (c) O 1s XPS spectra of TiO_2 and MnO_x/TiO_2 catalysts.

pristine TiO_2 or $Mn^{3+/2+}$ in MnO_x/TiO_2 catalysts.[43,46,48] The second peak around 529.1 eV corresponds to the adsorbed oxygenated species on oxygen vacancy sites (O_V). The peak around 531.3 eV belongs to the surface hydroxyl (O_{OH}) species in the catalysts. While the MnO_x/TiO_2 catalysts exhibited all three types of oxygen species; pristine TiO_2 materials did not display the O 1s peak of the O_{OH} species, which can function as Brønsted basic sites.

3.3. N_2 adsorption–desorption and CO_2-TPD studies of TiO_2 and MnO_x/TiO_2 nanocatalysts

Both pristine TiO_2 and MnO_x/TiO_2 nanocatalysts exhibited type IV isotherms with H3 hysteresis loops, indicative of slit-shaped pores/voids between the nanosized particles (Fig. S2, ESI†). Among the shape-controlled TiO_2 materials (Table S1, ESI†), the TiO_2-NS sample contains the highest BET surface area (198 $m^2\ g^{-1}$), followed by TiO_2-NT (185 $m^2\ g^{-1}$) and TiO_2-NR (129 $m^2\ g^{-1}$). MnO_x/TiO_2 nanocatalysts showed lower BET surface areas compared to their corresponding TiO_2 samples, which can be attributed to the aggregation of MnO_x particles and/or blockage of the slit-shaped pores/voids by MnO_x particles. The materials exhibited the average pore size and pore volume in the ranges of 25.06–26.18 nm and 0.288–0.604 $cm^3\ g^{-1}$, respectively (Table S1, ESI†).

Both the acid and base sites of the catalysts play a key role in the PET glycolysis reaction by activating the ester groups of PET and the alcohol group of EG, respectively.[33,36,43,55,56] Electron-deficient metal species like Ti^{4+} and Mn^{3+}/Mn^{2+} can activate the ester groups of the PET polymer. Although TiO_2 can show a mild Lewis acidic nature, its role is minimal in PET glycolysis, as all the TiO_2 materials showed very low activity compared with the MnO_x/TiO_2 catalysts (Table 1). The lattice oxygen (O^{2-}) and/or surface hydroxyl species of metal oxides can act as Lewis and Brønsted basic sites, respectively, which can accelerate the PET glycolysis by activating EG. Thus, we investigated the basic properties of these catalysts using the CO_2-TPD analysis (Fig. 6). All types of basic sites, namely weak (<200 °C), medium (200–400 °C), and strong (>400 °C) basic sites were found in the catalysts (Fig. 6a).[17,43] The MnO_x/TiO_2 catalysts showed a higher concentration of basic sites than the pristine TiO_2 materials (Fig. 6b). The surface hydroxyl species of MnO_x/TiO_2 catalysts (Fig. 5c), which are absent in TiO_2, likely contribute to the higher concentration of basic sites in MnO_x/TiO_2 catalysts. Among all the catalysts, the MnO_x/TiO_2-NR catalyst exhibited the highest concentration of basic sites (Fig. 6b), which could be the reason for its higher catalytic activity in PET glycolysis as discussed in the following sections.

3.4. Catalytic glycolysis of PET waste

3.4.1. Screening of TiO_2, MnO_x, and MnO_x/TiO_2 catalysts. The glycolysis of PET waste with EG was performed at 190 °C for 3 h. Without a catalyst (entry 1, Table 1), only 12% of PET was converted, and no BHET was formed. When shape-controlled TiO_2 nanomaterials were used, improved PET conversions and BHET yields were observed (entries 2–4, Table 1), revealing the catalytic role of TiO_2 in the PET glycolysis. The combination of MnO_x and TiO_2 resulted in significantly enhanced BHET yields (74–91%) with complete PET conversion (entries 5–7, Table 1). Among these, the MnO_x/TiO_2-NR catalyst showed the highest yield (91%) of BHET (entry 7, Table 1). When the amount of MnO_x/TiO_2-NR catalyst was reduced from 5 wt% to 3 wt%, both PET conversion (88%) and BHET yield (72%) decreased (entry 8, Table 1). Increasing the amount of MnO_x/TiO_2-NR catalyst to 7 wt% resulted in decreased yields of BHET (81%, entry 9, Table 1) compared to the 5 wt% MnO_x/TiO_2-NR catalyst (entry 7, Table 1). The com-

Table 1 PET glycolysis using various TiO_2, MnO_x, and MnO_x/TiO_2 catalysts

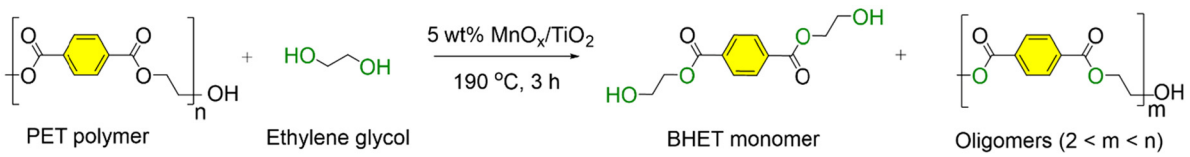

S. No.	Catalyst	PET conversion (%)	Isolated BHET yield (%)
1	Blank	12	Trace
2	TiO_2-NS[a]	76	14
3	TiO_2-NT	69	19
4	TiO_2-NR	74	17
5	MnO_x/TiO_2-NS	99	74
6	MnO_x/TiO_2-NT	99	82
7	MnO_x/TiO_2-NR	99	91
8	3 wt% MnO_x/TiO_2-NR	88	72
9	7 wt% MnO_x/TiO_2-NR	99	81
10	Commercial MnO_2[b]	99	67
11	Commercial MnO[b]	99	73
12	Commercial Mn_2O_3[b]	99	78

[a] Reaction conditions: 5 wt% of the catalyst concerning PET, 190 °C, 3 h, and 1 : 20 molar ratio of PET to EG. [b] SRL, 99.9% purity. Error in isolated BHET yield: ±3%.

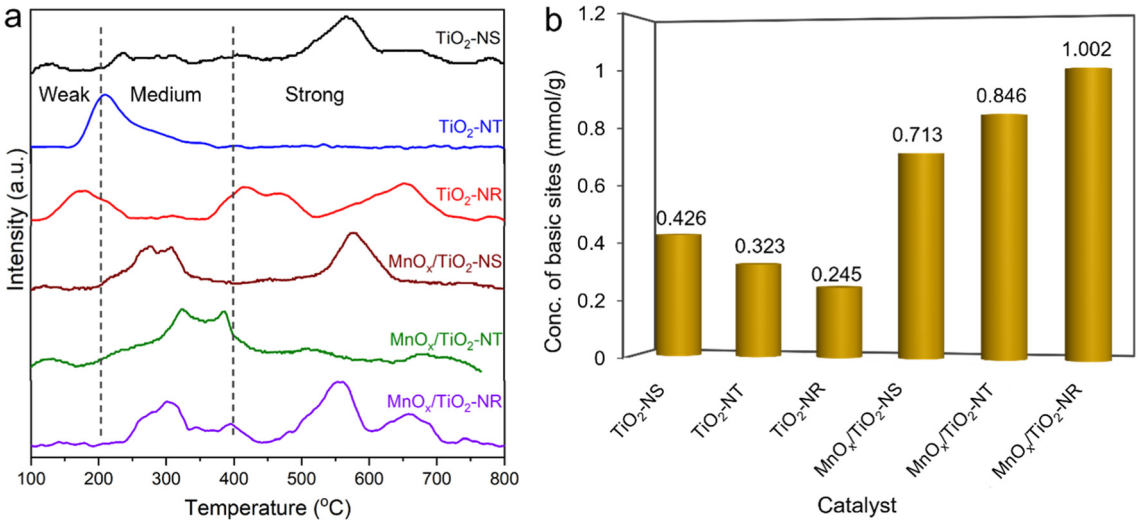

Fig. 6 (a) CO_2-TPD profiles and (b) basic site concentration of TiO_2 and MnO_x/TiO_2 catalysts.

mercial MnO_2 (entry 10, Table 1), MnO (entry 11, Table 1), and Mn_2O_3 (entry 12, Table 1) showed lower BHET yields compared to the MnO_x/TiO_2-NR catalyst (entry 7, Table 1). This underscores the importance of the developed nanostructured MnO_x/TiO_2-NR catalyst for optimizing BHET yields in PET glycolysis. Among the commercial manganese oxides, Mn_2O_3 (entry 12, Table 1) showed a higher BHET yield (78%), which indicates the importance of Mn^{3+} species in PET glycolysis. XPS studies showed the presence of a higher amount of Mn^{3+} species in the MnO_x/TiO_2-NR catalyst (Fig. 5a), contributing to its higher catalytic activity. The structure and molecular weight of the BHET monomer were confirmed by NMR (Fig. S3–S5, ESI†) and HR-MS (Fig. S6, ESI†) analyses.

3.4.2. Optimization of the reaction conditions. The optimization of various reaction conditions for PET glycolysis was conducted using a 5 wt% MnO_x/TiO_2-NR catalyst. The reaction temperature varying between 170 °C and 190 °C showed a steady increase in BHET yield, peaking at 91% at 190 °C (Fig. 7a). Beyond this temperature, a significant decline in BHET yield occurred, likely due to reverse reactions. The rapid solubility of PET in EG, which depends on the reaction conditions (EG amount, temperature, and time), is crucial for achieving higher conversion rates toward BHET production. The variation in EG concentration with PET as the limiting reagent (0.5 g) also had a notable effect on BHET yield (Fig. 7b). When the 1 : 12 molar ratio of PET : EG was taken, the PET chips were dissolved in EG over a period of 3 h at 190 °C, giving 89% PET conversion with 41% yield of BHET (Fig. 7b). A further increase of the EG amount (1 : 20 molar ratio of PET : EG) led to the rapid solubility of PET in EG, which can facilitate improved interaction of the catalyst's active sites with PET ester groups, giving 91% yield of BHET (Fig. 7b). Increasing the EG concentration beyond this ratio resulted in a decline in BHET yield. To determine the optimal reaction time, glycolysis of PET was carried out from 1 to 5 h in 30 min intervals (Fig. 7c). About 51% yield of BHET was attained with the 92% conversion of PET after 2 h. Further, an increase in the reaction time to 3 h led to the highest BHET yield (91%), but the backward reaction was initiated beyond 3 h.

3.4.3. PET glycolysis kinetics. The kinetic studies of PET glycolysis and the activation energy (E_a) values provide valuable insights for developing efficient PET recycling processes under mild reaction conditions. The reaction rate for the PET glycolysis was calculated by estimating the change in the PET concentration with time in a period of 3 h (Fig. 8a and b). As the PET is the limiting reagent, the reaction can be assumed to follow the first-order reaction such that $-dC_P/dt = kC_P$. Thus, the conversion, q, is related to the concentration as $q = [1 - (C_P/C_{P0})]$, where C_P and C_{P0} are the final and initial concentrations of PET, respectively. The logarithmic equation of PET conversion is plotted against time for the first-order reaction (Fig. 8b), representing the slope and intercept for the rate constant, which was found to be 0.0306 min^{-1}.[17,43]

The kinetic analysis of PET glycolysis was carried out using a 5 wt% MnO_x/TiO_2-NR catalyst at various reaction time intervals in a temperature range of 160 to 190 °C. The effect of reaction temperature with time was scrutinized using the kinetic plots for PET glycolysis (Fig. 8c). The rate constants obtained at various temperatures were then represented in an Arrhenius plot (Fig. 8d). Using the rate constants, the activation energy (E_a) could be obtained using following the equation.

$$\ln k = \ln A - E_a/RT$$

where A is the pre-exponential factor, R is the gas constant (8.314 J $kmol^{-1}$), and T is the temperature of the reaction in Kelvin.

The activation energy (E_a) was determined from the slope to be around 40 kJ mol^{-1} (Fig. 8d), which is much smaller than those reported in the literature. For instance, Schlüter *et al.* found the necessity of higher E_a (105 kJ mol^{-1}) for PET glycolysis at 190 °C over a zinc acetate catalyst using γ-valerolactone as a co-solvent.[57] In the case of Zn/Al mixed oxide, about

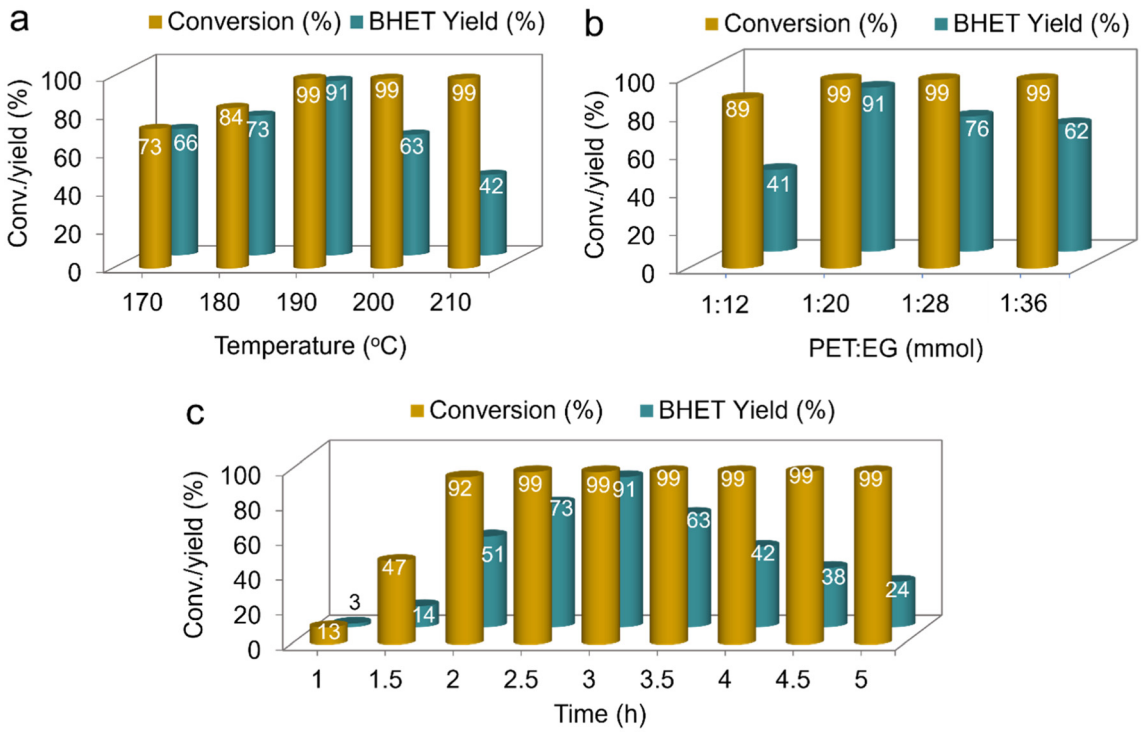

Fig. 7 Optimization of the reaction conditions for PET glycolysis using the MnO_x/TiO_2-NR catalyst: (a) temperature, (b) PET/EG molar ratio, and (c) reaction time. Reaction conditions: 1 : 20 molar ratio of PET : EG, 5 wt% MnO_x/TiO_2-NR catalyst, 190 °C, and 3 h. Error in isolated BHET yield: ±3%.

79.3 kJ mol^{-1} of E_a is needed to achieve an 82% yield of BHET under optimized reaction conditions.[58] Though FAU-type zeolite is active for PET glycolysis reaction, it requires a higher E_a value (233.9 kJ mol^{-1}) to obtain optimum yields of BHET.[59] The mineral basic catalyst *i.e.*, sodium carbonate showed an 80% yield of BHET at 196 °C for 1 h, and the E_a was estimated to be 185 kJ mol^{-1}.[60] The comparison of our results with the literature reports reveals that the MnO_x/TiO_2-NR catalyst is highly active for the PET glycolysis reaction with a much smaller E_a (40 kJ mol^{-1}) to obtain a 91% yield of BHET.

3.4.4. Hot-filtration and catalyst reusability studies. The stability of the MnO_x/TiO_2-NR catalyst was investigated by a hot filtration study (Fig. 9a). This large-scale reaction (2.5 g PET with a 1 : 20 molar ratio of PET : EG) was conducted at 190 °C for 3 h over the 5 wt% MnO_x/TiO_2-NR catalyst. A 58% yield of BHET was attained with the 99% conversion of PET after 1.5 h. Afterwards, the catalyst was removed from the reaction mixture by filtration, and the reaction continued for another 1.5 h. The variation in the BHET yield (62%) was negligible after the catalyst removal at 1.5 h, confirming the high stability of the MnO_x/TiO_2-NR catalyst without any leaching of the active sites (Fig. 9a).

The reusability of the MnO_x/TiO_2-NR catalyst for PET glycolysis was tested at 190 °C for 3 h with a 1 : 20 molar ratio of PET : EG using a 25 mg catalyst (5 wt% catalyst with respect to 0.5 g PET). The catalyst was reused for up to four cycles (Fig. 9b). About 20 mg of the catalyst was recovered after the reaction through filtration. To maintain the 25 mg catalyst for each cycle, we simultaneously carried out two batches of each reusability reaction, obtaining about 40 mg of the catalyst from two batches. The recovered catalyst was dried in an oven at 80 °C for 12 h, collected from the filter paper, washed with methanol to remove impurities, and then dried again at 80 °C for 12 h before calcination at 400 °C for 4 h. The calcined MnO_x/TiO_2-NR catalyst (25 mg) was used for the subsequent cycle. Only a small decrease in BHET yield was noticed after the 2nd (88%), 3rd (86%), and 4th (84%) cycles, demonstrating the catalyst's stability and consistent activity in PET glycolysis (Fig. 9b). The XPS analysis of the reused MnO_x/TiO_2-NR catalyst revealed that the peaks for both Mn^{2+} and Mn^{3+} were shifted to higher BEs compared to the fresh MnO_x/TiO_2-NR catalyst (Fig. S7a, ESI†). This shift is attributed to the participation of $Mn^{3+/2+}$ species in the PET glycolysis. However, the BEs of Ti^{4+} species remained consistent in both fresh and reused MnO_x/TiO_2-NR catalysts (Fig. S7b, ESI†), indicating their role is negligible in PET glycolysis. Adequate amounts of surface hydroxyl species were present in the reused MnO_x/TiO_2-NR catalyst (Fig. S7c, ESI†). The reused MnO_x/TiO_2-NR catalyst exhibited 0.921 mmol g^{-1} basic sites, whose concentration is 1.002 mmol g^{-1} in the fresh catalyst (Fig. 6b). Thus, the presence of adequate basic sites and surface hydroxyl species in the MnO_x/TiO_2-NR catalyst is the reason for its good reusability in PET glycolysis (Fig. 9b).

3.4.5. Structure–activity properties and a probable reaction mechanism. In PET glycolysis with EG, the basic sites on the catalyst surface abstract a proton from EG, enhancing its

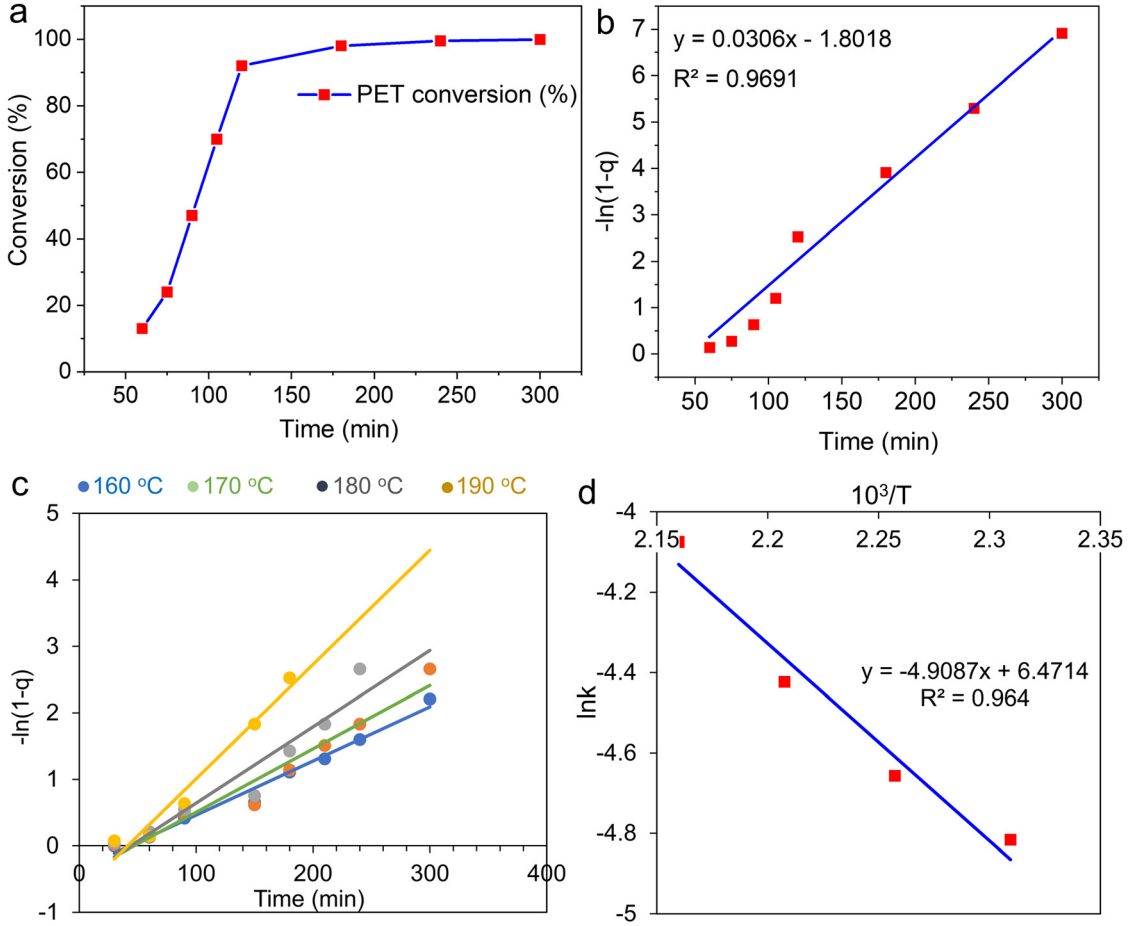

Fig. 8 (a) PET conversion with the reaction time, (b) the plot of $-\ln(1-q)$ with the reaction time ($q = 1 - C_P/C_{P0}$), (c) conversion of PET at different temperatures and time intervals, and (d) Arrhenius plot of the PET glycolysis reaction over the MnO_x/TiO_2-NR catalyst.

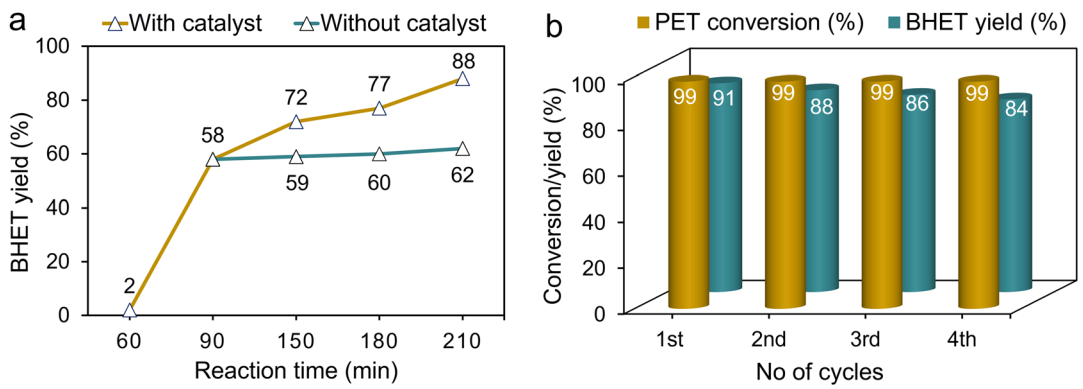

Fig. 9 (a) Hot filtration test of the MnO_x/TiO_2-NR catalyst for PET glycolysis (reaction conditions: 1 : 20 molar ratio of PET : EG, 5 wt% MnO_x/TiO_2-NR catalyst, 190 °C, and 3 h). (b) Reusability studies (reaction conditions: 1 : 20 molar ratio of PET : EG, 5 wt% MnO_x/TiO_2-NR catalyst, 190 °C, and 3 h). Error in isolated BHET yield: ±3%.

nucleophilicity to react with the ester linkages of PET, while metal sites can activate the carbonyl groups of PET, making them more susceptible to the nucleophilic attack of EG.[6,21,23,30,61,62] Pristine TiO_2 catalysts showed much lower yields of BHET than the corresponding MnO_x/TiO_2 catalysts (Table 1), which is due to the lack of adequate concentration of basic sites in TiO_2 (Fig. 6b). The presence of lower oxidation states of Mn (Mn^{2+} and Mn^{3+}) in MnO_x/TiO_2 catalysts can lead to the strong basic nature of lattice oxygen (O^{2-}), which activates EG by abstracting a proton from its alcohol groups. The

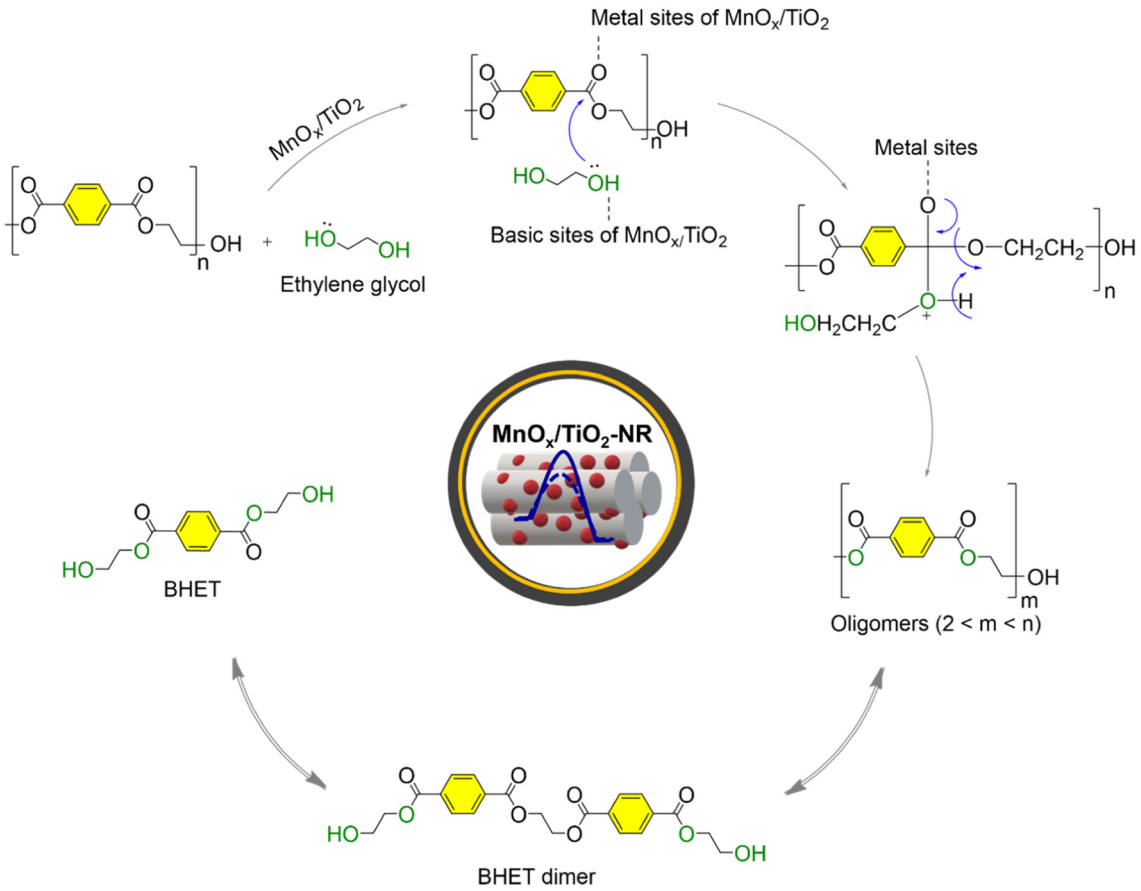

Fig. 10 A possible mechanism for the PET glycolysis reaction over the MnO_x/TiO_2-NR catalyst.

MnO_x/TiO_2-NR catalyst, with a higher concentration of basic sites (Fig. 6b) compared to MnO_x/TiO_2-NS and MnO_x/TiO_2-NT catalysts, demonstrates its superior catalytic performance for PET glycolysis (entry 7, Table 1). Based on these findings, a possible mechanism was proposed with the synergistic role of metal sites and basic sites in PET glycolysis (Fig. 10). This leads to the cleavage of PET ester linkages to yield oligomers, which further react with EG to produce BHET. The XPS studies showed that Mn^{2+} and Mn^{3+} sites in the MnO_x/TiO_2-NR catalyst shift to higher binding energies after the reaction (Fig. S7a, ESI†), indicating increased electron deficiency of these metal species because of their involvement in the glycolysis reaction. However, the BE of Ti^{4+} sites remains unchanged (Fig. S7b, ESI†), underscoring their stability during the reaction. The excellent stability and good reusability of the MnO_x/TiO_2-NR catalyst (Fig. 9) highlights its practical effectiveness in PET waste recycling to achieve optimum yields of the BHET monomer.

4. Conclusions

This study showed the effect of TiO_2 morphology on the structure–activity correlation of MnO_x/TiO_2 nanocatalysts for PET glycolysis. The combination of MnO_x with TiO_2 nanorods showed the highest yield of BHET compared with the corresponding TiO_2 nanosheet and nanotube-based MnO_x catalysts. The role of basic sites, surface hydroxyl species, and Mn^{3+}/Mn^{2+} in accelerating the PET glycolysis reaction is evident, elucidating the higher activity of the MnO_x/TiO_2-NR catalyst. The reaction rate and activation energy for PET glycolysis were estimated using kinetic studies at different reaction temperatures and time intervals. The MnO_x/TiO_2-NR catalyst was stable during the reaction, as investigated by the hot-filtration test, and the catalyst can be reused up to four times at least with complete conversion of PET while achieving good yields of BHET.

Data availability

The data supporting this article has been included as part of the ESI.†

Conflicts of interest

The authors declare no conflicts of interest.

Acknowledgements

B. S. is thankful to PMRF and MHRD for providing fellowship. P. S. acknowledges the funding support from MoE-STARS (Project ID: 2023-0038) and SERB (Project ID: CRG/2023/000197).

References

1 R. Geyer, J. R. Jambeck and K. L. Law, *Sci. Adv.*, 2017, **3**, e1700782, DOI: **10.1126/sciadv.1700782**.
2 T. Tan, W. Wang, K. Zhang, Z. Zhan, W. Deng, Q. Zhang and Y. Wang, *ChemSusChem*, 2022, **15**, e202200522, DOI: **10.1002/cssc.202200522**.
3 M. Chu, Y. Liu, X. Lou, Q. Zhang and J. Chen, *ACS Catal.*, 2022, **12**, 4659–4679, DOI: **10.1021/acscatal.2c01286**.
4 J. Huang, A. Veksha, W. P. Chan, A. Giannis and G. Lisak, *Renewable Sustainable Energy Rev.*, 2022, **154**, 111866, DOI: **10.1016/j.rser.2021.111866**.
5 G.-S. Ha, M. A. M. Rashid, D. H. Oh, J.-M. Ha, C.-J. Yoo, B.-H. Jeon, B. Koo, K. Jeong and K. H. Kim, *Waste Manage.*, 2024, **174**, 411–419, DOI: **10.1016/j.wasman.2023.12.028**.
6 S. Shirazimoghaddam, I. Amin, J. A. Faria Albanese and N. R. Shiju, *ACS Eng. Au*, 2023, **3**, 37–44, DOI: **10.1021/acsengineeringau.2c00029**.
7 R. A. Clark and M. P. Shaver, *Chem. Rev.*, 2024, **124**, 2617–2650, DOI: **10.1021/acs.chemrev.3c00739**.
8 H. Li, H. A. Aguirre-Villegas, R. D. Allen, X. Bai, C. H. Benson, G. T. Beckham, S. L. Bradshaw, J. L. Brown, R. C. Brown, V. S. Cecon, J. B. Curley, G. W. Curtzwiler, S. Dong, S. Gaddameedi, J. E. García, I. Hermans, M. S. Kim, J. Ma, L. O. Mark, M. Mavrikakis, O. O. Olafasakin, T. A. Osswald, K. G. Papanikolaou, H. Radhakrishnan, M. A. Sanchez Castillo, K. L. Sánchez-Rivera, K. N. Tumu, R. C. Van Lehn, K. L. Vorst, M. M. Wright, J. Wu, V. M. Zavala, P. Zhou and G. W. Huber, *Green Chem.*, 2022, **24**, 8899–9002, DOI: **10.1039/D2GC02588D**.
9 D. Sajwan, A. Sharma, M. Sharma and V. Krishnan, *ACS Catal.*, 2024, **14**, 4865–4926, DOI: **10.1021/acscatal.2c02292**.
10 A. K. Manal, A. Shivhare, S. Lande and R. Srivastava, *Chem. Commun.*, 2024, **60**, 13143–13168, DOI: **10.1039/D4CC03261F**.
11 Q. Liu, S. Martinez-Villarreal, S. Wang, N. Ngoc Thanh Tien, M. Kammoun, Q. De Roover, C. Len and A. Richel, *Chem. Eng. J.*, 2024, **498**, 155227, DOI: **10.1016/j.cej.2024.155227**.
12 T. Ren, H. Zhan, H. Xu, L. Chen, W. Shen, Y. Xu, D. Zhao, Y. Shao and Y. Wang, *Environ. Res.*, 2024, **249**, 118428, DOI: **10.1016/j.envres.2024.118428**.
13 T. Muringayil Joseph, S. Azat, Z. Ahmadi, O. Moini Jazani, A. Esmaeili, E. Kianfar, J. Haponiuk and S. Thomas, *Case Stud. Chem. Environ. Eng.*, 2024, **9**, 100673, DOI: **10.1016/j.cscee.2024.100673**.
14 C. Jehanno, M. M. Pérez-Madrigal, J. Demarteau, H. Sardon and A. P. Dove, *Polym. Chem.*, 2019, **10**, 172–186, DOI: **10.1039/C8PY01284A**.
15 Z. Gao, B. Ma, S. Chen, J. Tian and C. Zhao, *Nat. Commun.*, 2022, **13**, 3343, DOI: **10.1038/s41467-022-31078-w**.
16 R. A. Sheldon and M. Norton, *Green Chem.*, 2020, **22**, 6310–6322, DOI: **10.1039/D0GC02630A**.
17 B. Swapna, S. B. Putla, A. Ramesh, C. Subrahmanyam, G. Madras and P. Sudarsanam, *Sustainable Energy Fuels*, 2024, **8**, 5170–5180, DOI: **10.1039/D4SE01136H**.
18 J. Payne and M. D. Jones, *ChemSusChem*, 2021, **14**, 4041–4070, DOI: **10.1002/cssc.202100400**.
19 M. Rabnawaz, I. Wyman, R. Auras and S. Cheng, *Green Chem.*, 2017, **19**, 4737–4753, DOI: **10.1039/C7GC02521A**.
20 K. R. Delle Chiaie, F. R. McMahon, E. J. Williams, M. J. Price and A. P. Dove, *Polym. Chem.*, 2020, **11**, 1450–1453, DOI: **10.1039/C9PY01920K**.
21 N. George and T. Kurian, *Ind. Eng. Chem. Res.*, 2014, **53**, 14185–14198, DOI: **10.1021/ie501995m**.
22 S. Lalhmangaihzuala, Z. Laldinpuii, C. Lalmuanpuia and K. Vanlaldinpuia, *Polymers*, 2020, **13**, 37, DOI: **10.3390/polym13010037**.
23 A. Bohre, P. R. Jadhao, K. Tripathi, K. K. Pant, B. Likozar and B. Saha, *ChemSusChem*, 2023, **16**, e202300142, DOI: **10.1002/cssc.202300142**.
24 K. Kumari, P. Choudhary and V. Krishnan, *Catal. Sci. Technol.*, 2024, **14**, 5352–5363, DOI: **10.1039/D4CY00468J**.
25 T. D. J. te Molder, S. R. A. Kersten, J. P. Lange and M. P. Ruiz, *Ind. Eng. Chem. Res.*, 2021, **60**, 7043–7049, DOI: **10.1021/acs.iecr.1c01063**.
26 H. Xin, H. Wang, S. Li, X. Hu, C. Wang, L. Ma and Q. Liu, *Sustainable Energy Fuels*, 2022, **6**, 2602–2612, DOI: **10.1039/D2SE00386D**.
27 A. Wang and T. Zhang, *Acc. Chem. Res.*, 2013, **46**, 1377–1386, DOI: **10.1021/ar3002156**.
28 Q. Wang, X. Yao, S. Tang, X. Lu, X. Zhang and S. Zhang, *Green Chem.*, 2012, **14**, 2559–2566, DOI: **10.1039/C2GC35696A**.
29 N. H. Le, T. T. Ngoc Van, B. Shong and J. Cho, *ACS Sustainable Chem. Eng.*, 2022, **10**, 17261–17273, DOI: **10.1021/acssuschemeng.2c05570**.
30 B. Liu, W. Fu, X. Lu, Q. Zhou and S. Zhang, *ACS Sustainable Chem. Eng.*, 2019, **7**, 3292–3300, DOI: **10.1021/acssuschemeng.8b05324**.
31 Z. Wang, Y. Jin, Y. Wang, Z. Tang, S. Wang, G. Xiao and H. Su, *ACS Sustainable Chem. Eng.*, 2022, **10**, 7965–7973, DOI: **10.1021/acssuschemeng.2c01235**.
32 D. Lei, X.-L. Sun, S. Hu, H. Cheng, Q. Chen, Q. Qian, Q. Xiao, C. Cao, L. Xiao and B. Huang, *Ind. Eng. Chem. Res.*, 2022, **61**, 4794–4802, DOI: **10.1021/acs.iecr.1c05022**.
33 A. M. Al-Sabagh, F. Z. Yehia, D. R. K. Harding, Gh. Eshaq and A. E. ElMetwally, *Green Chem.*, 2016, **18**, 3997–4003, DOI: **10.1039/C6GC00534A**.
34 G. Park, L. Bartolome, K. G. Lee, S. J. Lee, D. H. Kim and T. J. Park, *Nanoscale*, 2012, **4**, 3879–3885, DOI: **10.1039/C2NR30168G**.
35 M. R. Nabid, Y. Bide and M. Jafari, *Polym. Degrad. Stab.*, 2019, **169**, 108962, DOI: **10.1016/j.polymdegradstab.2019.108962**.
36 Z. Fehér, J. Kiss, P. Kisszékelyi, J. Molnár, P. Huszthy, L. Kárpáti and J. Kupai, *Green Chem.*, 2022, **24**, 8447–8459, DOI: **10.1039/D2GC02860C**.

37 F. Tanos, A. Razzouk, G. Lesage, M. Cretin and M. Bechelany, *ChemSusChem*, 2024, **17**, e202301139, DOI: **10.1002/cssc.202301139**.
38 T. Kim, H. Nguyen-Phu, T. Kwon, K. H. Kang and I. Ro, *Environ. Pollut.*, 2023, **331**, 121876, DOI: **10.1016/j.envpol.2023.121876**.
39 M. Ge, C. Cao, J. Huang, S. Li, Z. Chen, K.-Q. Zhang, S. S. Al-Deyab and Y. Lai, *J. Mater. Chem. A*, 2016, **4**, 6772–6801, DOI: **10.1039/C5TA09323F**.
40 P. Sudarsanam, H. Li and T. V. Sagar, *ACS Catal.*, 2020, **10**, 9555–9584, DOI: **10.1021/acscatal.0c01680**.
41 Y. Zou, M. Zhang, F. Cao, J. Li, S. Zhang and Y. Qu, *J. Mater. Chem. A*, 2021, **9**, 19692–19697, DOI: **10.1039/D1TA04415J**.
42 C. Liu, Q. Hu, Q. Chen, J. Wang, L. Zhang and Y. Ni, *J. Cluster Sci.*, 2018, **29**, 185–194, DOI: **10.1007/s10876-017-1320-z**.
43 B. Swapna, N. Singh, S. Patowary, P. Bharali, G. Madras and P. Sudarsanam, *Catal. Sci. Technol.*, 2024, **14**, 5574–5587, DOI: **10.1039/D4CY00823E**.
44 M. E. Viana, A. Riul, G. M. Carvalho, A. F. Rubira and E. C. Muniz, *Chem. Eng. J.*, 2011, **173**, 210–219, DOI: **10.1016/j.cej.2011.07.031**.
45 Y. Liu, P. Fang, Y. Cheng, Y. Gao, F. Chen, Z. Liu and Y. Dai, *Chem. Eng. J.*, 2013, **219**, 478–485, DOI: **10.1016/j.cej.2012.12.098**.
46 P. Sudarsanam, A. Köckritz, H. Atia, M. H. Amin and A. Brückner, *ChemCatChem*, 2021, **13**, 1990–1997, DOI: **10.1002/cctc.202001870**.
47 Y. Wang, Z. Lu, P. Wen, Y. Gong, C. Li, L. Niu and S. Xu, *Nanoscale*, 2023, **15**, 17850–17860, DOI: **10.1039/D3NR04274J**.
48 N. Singh, S. B. Putla, C. Pratap Singh, P. N. Kalbande, P. Choudhary, S. Krishnamurty, V. Krishnan, K. Bhatte and P. Sudarsanam, *ACS Appl. Nano Mater.*, 2023, **6**, 23442–23453, DOI: **10.1021/acsanm.3c04820**.
49 Y. X. Zhang, X. D. Hao, F. Li, Z. P. Diao, Z. Y. Guo and J. Li, *Ind. Eng. Chem. Res.*, 2014, **53**, 6966–6977, DOI: **10.1021/ie5002229**.
50 J. Li, J. Chen, R. Ke, C. Luo and J. Hao, *Catal. Commun.*, 2007, **8**, 1896–1900, DOI: **10.1016/j.catcom.2007.03.007**.
51 G. Qi and R. T. Yang, *Appl. Catal., B*, 2003, **44**, 217–225, DOI: **10.1016/S0926-3373(03)00100-0**.
52 D. Song, X. Shao, M. Yuan, L. Wang, W. Zhan, Y. Guo, Y. Guo and G. Lu, *RSC Adv.*, 2016, **6**, 88117–88125, DOI: **10.1039/C6RA20999H**.
53 A. Sathe, M. A. Peck, C. Balasanthiran, M. A. Langell, R. M. Rioux and J. D. Hoefelmeyer, *Inorg. Chim. Acta*, 2014, **422**, 8–13, DOI: **10.1016/j.ica.2014.08.011**.
54 J. Liu, B. Liu, Y. Ren, Y. Yuan, H. Zhao, H. Yang and S. (Frank) Liu, *J. Mater. Chem. A*, 2019, **7**, 14761–14775, DOI: **10.1039/C9TA00736A**.
55 D. Thomas, R. Ranjan and B. K. George, *RSC Sustainability*, 2023, **1**, 2277–2286, DOI: **10.1039/D3SU00304C**.
56 S. Najmi, B. C. Vance, E. Selvam, D. Huang and D. G. Vlachos, *Chem. Eng. J.*, 2023, **471**, 144712, DOI: **10.1016/j.cej.2023.144712**.
57 M. Schlüter, S. Bhutani, K. Wohlgemuth and C. Held, *Ind. Eng. Chem. Res.*, 2024, **63**, 15458–15465, DOI: **10.1021/acs.iecr.4c02382**.
58 F. Chen, Q. Zhou, R. Bu, F. Yang and W. Li, *Fibers Polym.*, 2015, **16**, 1213–1219, DOI: **10.1007/s12221-015-1213-4**.
59 G. Yang, H. Wu, K. Huang, Y. Ma, Q. Chen, Y. Chen, S. Lin, H. Guo and Z. Li, *J. Polym. Environ.*, 2024, **32**, 5071–5085, DOI: **10.1007/s10924-024-03298-2**.
60 R. López-Fonseca, I. Duque-Ingunza, B. de Rivas, L. Flores-Giraldo and J. I. Gutiérrez-Ortiz, *Chem. Eng. J.*, 2011, **168**, 312–320, DOI: **10.1016/j.cej.2011.01.031**.
61 L. O. Mark, M. C. Cendejas and I. Hermans, *ChemSusChem*, 2020, **13**, 5808–5836, DOI: **10.1002/cssc.202001905**.
62 S. Javed and D. Vogt, *ACS Sustainable Chem. Eng.*, 2023, **11**, 11541–11547, DOI: **10.1021/acssuschemeng.3c01872**.